https://doi.org/10.5194/egusphere-2026-4353
Preprint. Discussion started: 11 August 2026

A cost-effective, open source, high resolution visible wavelength camera network: design and applications for long-term monitoring and research in volcanology

Riccardo Simionato[1,2], Allan Fries[1], Simon Thivet[3,1], Jonathan Lemus[1,2], Carolina Díaz-Vecino[1], Frederic Arlaud[1], Simona Scollo[4], and Costanza Bonadonna[1]

[1]Department of Earth Sciences, University of Geneva, Geneva, Switzerland
[2]Department of Computer Science, University of Geneva, Carouge, Switzerland
[3]Department of Geosciences, University of Fribourg, Fribourg, Switzerland
[4]Istituto Nazionale di Geofisica e Vulcanologia, Osservatorio Etneo, Catania, Italy

Correspondence: Riccardo Simionato (Riccardo.Simionato@unige.ch) and Costanza Bonadonna (Costanza.Bonadonna@unige.ch)

Abstract. Monitoring and forecasting volcanic processes are crucial for detecting, characterising, and assessing associated hazards. However, advanced monitoring tools, such as thermal cameras, can be expensive and unavailable in many monitoring networks. To address this, a cost-effective visible wavelength camera network has been developed to capture high resolution imagery for volcano monitoring and research.

This network provides continuous, automated image acquisition from different locations around a volcanic edifice. Each camera node is equipped with a Raspberry Pi computer board, one or two Raspberry Pi Camera Module 3 cameras, and a waterproof and dustproof box for deployment in challenging outdoor environments, with an estimated cost of approximately EUR 152-257 per unit, depending on the hardware configuration. The system supports diverse configurations, including adjustable capture intervals and resolutions, to meet various observational needs. The network adapts its operation based on environmental conditions, automatically selecting the shutter speed during daylight and using specific settings at night. Acquired data can be transferred in near real time to a server for archival and, potentially, analysis for monitoring purposes.

In this study, we present a long-term camera monitoring network deployed at Mt. Etna, together with short-term deployments at Stromboli, the Geneva Jet d'Eau as a calibrated experiment, and laboratory experiments. These case studies demonstrate the long-term reliability of the system for capturing images over extended periods under variable lighting and weather conditions, including high temperatures, snow, rain, and tephra fallout, as well as its suitability as a temporary observation tool for field campaigns or laboratory setups. By using open source hardware and software, this camera network provides a flexible and accessible tool for volcano monitoring and research applications. When paired with cellular connectivity and solar panels or battery packs, the system could be integrated into multisensor monitoring networks, including in remote areas and challenging outdoor environments. Although developed for volcano monitoring, the framework can be adapted to other natural and environmental processes requiring persistent or high temporal resolution visual observations.

https://doi.org/10.5194/egusphere-2026-4353
Preprint. Discussion started: 11 August 2026

1 Introduction

Volcanic eruptions present significant hazards to local populations (Horwell and Baxter, 2006; Stewart et al., 2006; Wilson et al., 2011; Phillips et al., 2019), infrastructure (Spence et al., 2005; Wilson et al., 2012), and air traffic (Guffanti et al., 2009, 2010; Clarkson, 2017), making effective monitoring essential for early warning and risk mitigation. Visible wavelength cameras are commonly deployed as monitoring devices on volcanoes (e.g., Scollo et al., 2014; Patrick et al., 2015; Barnie et al., 2023) and are widely recognised as essential tools by volcano observatories and research institutions, regardless of their intrinsic limitations (i.e., cloud coverage and lighting conditions). Continuous visual observation of active volcanoes makes it possible to identify potential activity, classify phenomena, and obtain quantitative measurements, which are of paramount importance for assessing volcanic hazards. These include measurements of plume heights, geometry, and rise rates (Arason et al., 2011; Scollo et al., 2014; Valade et al., 2014; Simionato et al., 2024), ballistic trajectories (Taddeucci et al., 2017; Sork et al., 2024), tephra sedimentation (Manzella et al., 2015; Fries et al., 2026a), air entrainment (Mingotti and Woods, 2024), incandescence as a proxy for active lava flows or activity levels at open vents (Patrick et al., 2010), and pyroclastic density currents flow rates (Kilgour et al., 2019). In particular, plume height is a fundamental parameter, as high frequency data are needed for finding relationships with the mass eruption rate (MER) (e.g., Mastin et al., 2009; Degruyter and Bonadonna, 2012; Woodhouse et al., 2013; de Michele et al., 2016; Dürig et al., 2018; Aubry et al., 2023), which is ultimately used as an input parameter for simulating volcanic ash transport and dispersal. Visible imagery is also important for effusive activity, as repeated observations can document lava flow emplacement and provide constraints on flow front position, propagation rate, and interaction with the surrounding terrain (Patrick et al., 2019; Coltelli et al., 2017). However, high resolution imagery monitoring networks are often limited to a few volcanoes, due to the high cost of commercial webcam systems, maintenance requirements, and logistical difficulties associated with deploying and operating advanced imaging systems in remote or hazardous environments. This limitation is particularly relevant in the context of increasing use of automated and artificial intelligence based image analysis, because training datasets are not necessarily transferable from one volcano to another (Diaz et al., 2021; Wilkes et al., 2022). Expanding image acquisition to a broader range of volcanoes, including less monitored systems, is therefore important for building more representative datasets. The aforementioned limitations create a clear need for more accessible, adaptable monitoring tools that can complement existing networks or serve as standalone systems in under instrumented settings. Combined with open source software, these tools can provide surprisingly robust alternatives to proprietary sensors and monitoring systems, offering high resolution imaging capabilities, programmable control, and remote connectivity at a fraction of the cost. Beyond long-term monitoring, rapidly deployable cameras are therefore useful during field campaigns and laboratory experiments, where flexible acquisition settings can be adapted to short-lived or rapidly evolving processes.

In the last decade, the growing availability of cost-effective, low power embedded systems has enabled the development of custom sensing solutions using consumer grade hardware. Particularly, small-sized single board computers, like Raspberry Pi (raspberrypi.com), represent the ideal platform for a wide range of scientific applications, including data acquisition, control systems, and low resources demanding modelling, spanning a wide range of disciplines, including environmental sciences, engineering, computer science, physics, astronomy, biochemistry, genetics and molecular biology, materials science, and chem-

https://doi.org/10.5194/egusphere-2026-4353
Preprint. Discussion started: 11 August 2026

istry (Mathe et al., 2024). Yet, despite their potential, their use in volcanology remains underexploited, with few studies using Raspberry Pi computer boards as gateway node (Ricco et al., 2018; Awadallah et al., 2019; Catalan et al., 2020; Hidayatullah et al., 2020), controller for instruments (Moure et al., 2015; Anthony et al., 2018; Pering et al., 2024; Prata et al., 2024; Clive et al., 2024), and for unoccupied vehicles (Parcheta et al., 2016). The opportunity to be coupled with Raspberry Pi Camera Modules (also referenced as PiCams hereafter) widens even more its possible applications, from experimental measurements (e.g., Miikki et al., 2021; Sarıyer et al., 2023), to surveillance (e.g., Abaya et al., 2014; Nguyen et al., 2015) and monitoring (e.g., Prinz et al., 2016; Kirby et al., 2018; Wilkinson et al., 2021) systems (see also Mathe et al., 2024, for a complete review of applications, with or without PiCams). Applications to volcanological studies with the PiCams include: the characterisation of ground deposited (Andò et al., 2022) or airborne sampled (Thivet et al., 2025) volcanic ash; the modification of the camera itself through chemical treatments and filter application to work in the ultraviolet and infrared spectrum (Wilkes et al., 2016) to make SO_2 emission measurements (Wilkes et al., 2017, 2019; Ilanko et al., 2020) and thermal imaging (Wilkes et al., 2018); and volcano monitoring (Patrick et al., 2015; Barnie et al., 2023). Indeed, the only applications to visible wavelength volcano monitoring have been made by the U.S. Geological Survey Hawaiian Volcano Observatory (Patrick et al., 2015) and the Icelandic Meteorological Office (Barnie et al., 2023). In their work, Patrick et al. (2015) describe the use of a Raspberry Pi based camera system for field deployment at active volcanoes that can be used either as a long- or short-term monitoring camera during field visits. Notwithstanding the open source nature of their work, hardware, and software have advanced significantly in the last decade, rendering their approach outdated for current use. On the contrary, Barnie et al. (2023) used several webcam types, including PiCams, to build their network around Fagradalsfjall volcano. However, their focus is mainly on the calibration of the system to manually retrieve plume heights during the 2021 Fagradalsfjall eruption through a specific software, and, even if providing broad instructions for the construction of the system, their codes are only available upon request.

In this study, we present the development and field implementation of a network of open source, cost-effective, high resolution visible wavelength camera nodes based on Raspberry Pi products and designed for continuous volcano monitoring. Hereafter, a camera node refers to a self-contained unit comprising a camera module, embedded computer, and on node scheduling software. The system is fully customizable, enabling adjustments to image resolution, capture interval, and shutter settings, but also to how acquired data are handled and transferred in quasi real time. One of the main objectives of this work is to provide end users with access to the developed system, including the necessary code and detailed instructions for its use (Sect. 2 and Simionato, 2026). Moreover, the camera nodes have been deployed and tested at different locations, where the system has proven reliable under a wide range of conditions, including extreme temperatures, atmospheric precipitation, and ash fallout (Sect. 3). The system simplicity, adaptability, and affordability make it particularly suitable for use by volcano observatories with limited resources, as well as for field campaigns, allowing rapid deployment and minimal maintenance (Sect. 4-5).

https://doi.org/10.5194/egusphere-2026-4353
Preprint. Discussion started: 11 August 2026

2 Materials and methods

2.1 Hardware and design of the camera nodes

Each camera node is based on a Raspberry Pi computer board and a Raspberry Pi Camera Module 3. To adapt our camera nodes to different purposes, we set up different hardware configurations with Raspberry Pi 4 Model B and Raspberry Pi 5, along with different cameras.

The Raspberry Pi 4 Model B (1GB RAM) is equipped with a quad core 64-bit processor (Broadcom BCM2711 - Quad core Cortex-A72 ARM v8 64-bit SoC @ 1.8GHz), a 1GB random access memory (RAM; LPDDR4-3200 SDRAM), 2.4 GHz and 5.0 GHz wireless, two universal serial bus (USB) 2.0 and two USB 3.0 ports, a Gigabit Ethernet port (with enabled Power over Ethernet, requiring additional PoE HAT), and a 2-lane MIPI CSI camera port (see full Raspberry Pi 4 Model B specifications).

The newer Raspberry Pi 5 (2GB RAM) features a quad core 64-bit processor (Broadcom BCM2712 - Quad core Cortex-A76 ARM v8.2-A SoC @ 2.4GHz), a 2GB RAM (LPDDR4X-4267 SDRAM), 2.4 GHz and 5.0 GHz wireless networking, two USB 2.0 and two USB 3.0 ports (supporting simultaneous high speed connections), a Gigabit Ethernet port (with optional PoE via a separate PoE+ HAT), and two 4-lane MIPI CSI/DSI ports for cameras and displays (see full Raspberry Pi 5 specifications).

The Raspberry Pi Camera Module 3 series is available in four variants: Standard, Wide, NoIR Standard, and NoIR Wide. All models feature a 12-megapixel Sony IMX708 back illuminated CMOS sensor with autofocus capability, for a maximum resolution of 4608×2592 pixels and 1080p50, 720p100, 480p120 video modes. The Standard versions have a horizontal field of view of $66°$, while the Wide versions extend this to around $102°$, using a different lens. NoIR models omit the infrared filter, making them suitable for low light and night imagery (see full Raspberry Pi Camera Module 3 specifications and documentation).

All electronic components are enclosed in a weatherproof housing for short- to long-term deployment in harsh outdoor environments. Since the enclosure is IP65-rated (dust tight and protected against water jets), air circulation is not possible. To ensure adequate CPU cooling, the appropriate Raspberry Pi cooling system (thermal pads, heatsinks, and fan) is installed to homogenize the temperature inside the box (tests showed the thermal pad and heatsink alone lower the CPU temperature by approximately $5 - 10\,°C$ in a $20\,°C$ ambient environment). The only cable exiting the box is for the power supply, passing through an IP68 cable gland. The Raspberry Pi board and camera are mounted through the designated holes onto a custom designed, 3D printed plastic holder (with M2 screws and nuts), which is snap fitted to the box.

Two specific configurations, using the hardware components described above, have been conceived and tested depending on their application (Fig. 1):

- For long-term monitoring networks, we use a Raspberry Pi 5, which is provided with two MIPI CSI/DSI ports allowing the simultaneous connection of a PiCam 3 Std and a PiCam3 NoIR (Fig. 1a). The operating system (Raspberry Pi OS 64-bit, based on Debian Bookworm) is installed on a solid state drive (Raspberry Pi 256GB NVMe SSD), which is mounted on a Raspberry Pi M.2 HAT+ and connected to the main board through a ribbon cable. Power is provided through the dedicated proprietary Raspberry Pi power supply. The total cost of this configuration is approximately EUR 257 (Table 1).

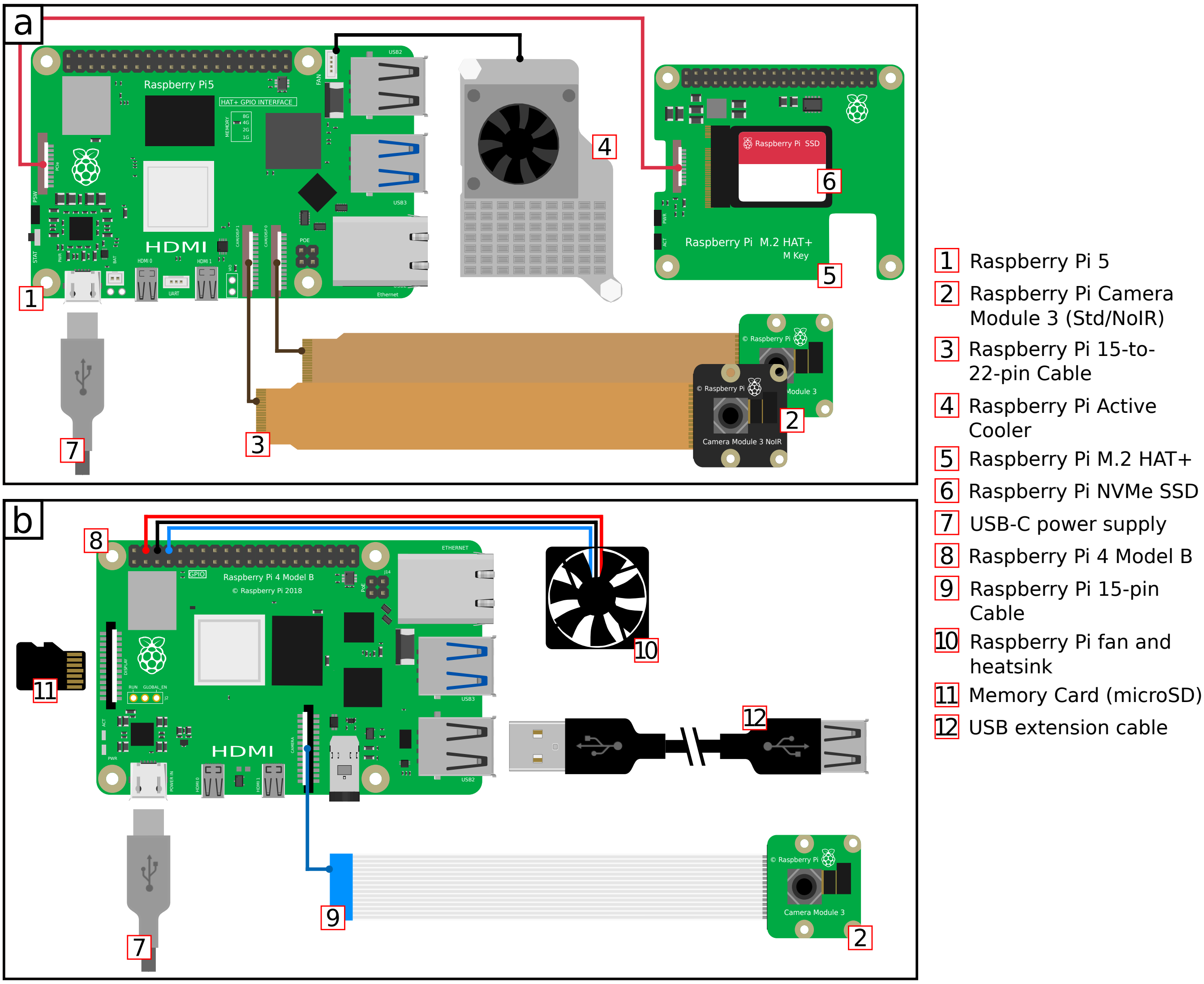

Figure 1. Schematic representation of all electronic components for (a) the long-term configuration and (b) the temporary configuration.

- For temporary configurations and laboratory settings, we use a Raspberry Pi 4 Model B equipped with a PiCam 3 Std (Fig. 1b). The operating system (Raspberry Pi OS 64-bit, based on Debian Bookworm) is installed on a microSD memory card (SanDisk Extreme microSDXC A2 U3 UHS-I168 V30, 128GB). A USB extension cable is connected and passed outside the weatherproof box to allow physical data transfer to an external drive in conditions at which wireless transfer is not available. Power is provided through the dedicated proprietary Raspberry Pi power supply, when grid power is available, or through power banks. The total cost of this configuration is approximately EUR 152 (Table 1).

https://doi.org/10.5194/egusphere-2026-4353
Preprint. Discussion started: 11 August 2026

Table 1. Cost and specifications of each component for one camera node with a long-term (L) or temporary (T) configuration. Prices are listed in EUR from official resellers as of June 2026, excluding value added tax (VAT). As an example, an approximate VAT inclusive total is also reported by applying the mean standard VAT rate of euro area EU member states ($\sim 21.45\,\%$).

Description	**Component specifications**	**Price (EUR)**	
		L	**T**
Computer board	Raspberry Pi 5 2GB RAM	60	
	Raspberry Pi 4 Model B 1GB RAM		33
Camera and cable	Raspberry Pi Camera Module 3	24	24
	Raspberry Pi Camera Module 3 NoIR	23	
Fan and heatsink	Raspberry Pi Active Cooler	5	
	Raspberry Pi 4 Case Fan and Heatsink		4
Power supply	Raspberry Pi 27W USB-C Power Supply 5V/5A	9	
	Raspberry Pi 15W USB-C Power Supply 5V/3A		6
OS storage unit	Raspberry Pi NVMe SSD 256GB with M.2 HAT+	77	
	SanDisk Extreme microSDXC A2 U3 V30 128GB		39
Transfer cable	Amazon Basics USB-A 3.0 extension cable		5
Weatherproof box	Bud Industries Electrical Enclosure IP65	13	13
Cable gland	Cable gland IP68 6-12 mm	<1	<1
Plastic holder	In house designed and 3D printed	<1	<1
Screws and nuts	Stainless steel M2 screws and nuts	<1	<1
Total	**excl. VAT**	**212**	**125**
	incl. 21.45% VAT (mean standard euro area EU rate)	**257**	**152**

A comprehensive guide to the installation and assembly of the camera node is provided in Simionato (2026, see rpicamnodes/README.md).

2.2 Software and workflow

The camera nodes operate with a lightweight software stack based on Bash scripts managed through `cron` and standard Linux services. Here, we provide a general and concise overview of the operational logic, as different configurations may require specific setups (see rpicamnodes/README.md for more details on scheduling rules and implementation). An initial interactive setup script is used to configure system parameters (e.g., time zone, Wi-Fi/WLAN, remote access) and node specific acquisition settings (e.g., capture mode and sampling interval), as well as optional data transfer and notification features. After setup, the node runs unattended and performs continuous image (or video) acquisition, local archiving, optional transfer to a remote server, and basic self recovery (Fig. 2). Image and video acquisition is handled through `rpicam-still` (or `rpicam-vid`)

https://doi.org/10.5194/egusphere-2026-4353
Preprint. Discussion started: 11 August 2026

and the output is organised into date stamped directories. Capture parameters for image acquisition (notably shutter speed and sampling interval) are automatically adjusted as a function of illumination (day, twilight, night) using location dependent sunrise and sunset times computed with `sunwait` (Risacher and Craig, 2022). Therefore, during twilight and night, the sampling interval is progressively increased. A watchdog script is executed periodically to check that the acquisition process is running (and restart it if required). When enabled, it also checks network connectivity and triggers `rsync` data transfer to a remote server. Local files are automatically removed only after a successful transfer. Optional capabilities include email notifications (SMTP) and automatic offloading to a USB storage device upon mounting. In addition, a scheduled daily reboot is used as a preventive measure against rare long uptime failures that may not be solved by the watchdog.

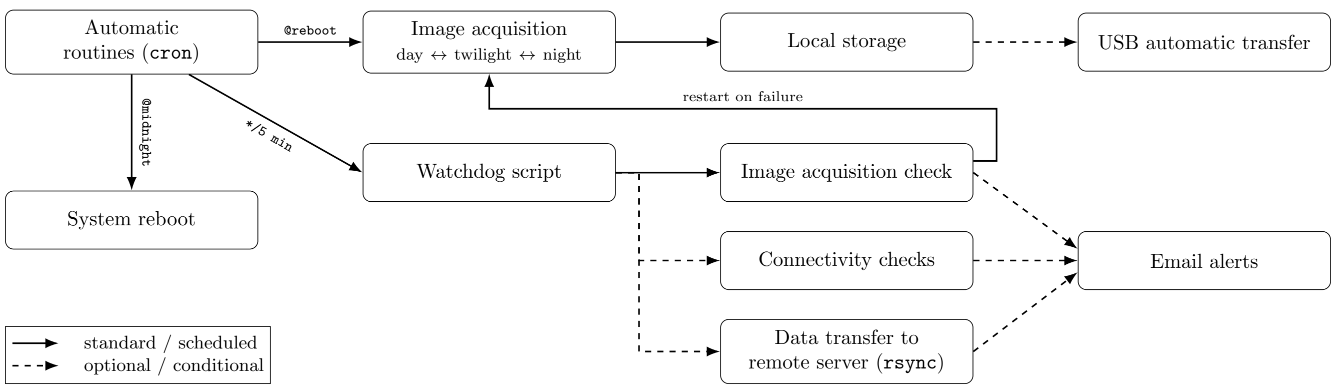

Figure 2. Simplified workflow of a camera node. Scheduled operations are represented by solid arrows, while optional and/or conditional operations are represented by dashed arrows.

2.3 Deployment of camera nodes network

The camera nodes have been tested and deployed at several locations in different configurations depending on the application and purpose of the recording. For temporary installations, the acquisition loop starts automatically after boot and can run unattended, with all outputs archived locally. Depending on site constraints, data can be retrieved either through wireless transfer or by manual offloading from local storage (e.g., via USB or `rsync`/`scp`). This configuration supports both still image timelapse acquisition at short sampling intervals and video acquisition at standard or high frame rates, allowing the same node to be used during field campaigns, short-term experiments, or as support to other instruments.

2.3.1 Mt. Etna (Italy)

The first version of a long-term monitoring network was installed at Mt. Etna (Italy) in September 2024. At that time, the hardware consisted of a Raspberry Pi 4 in a configuration similar to the one now dedicated to temporary uses. Therefore, to exploit both daylight and night vision, two separate camera nodes were necessary. Camera nodes were installed at three locations around Mt. Etna to study sedimentation from volcanic clouds. These sites are located on private properties in Adrano

https://doi.org/10.5194/egusphere-2026-4353
Preprint. Discussion started: 11 August 2026

(A; at 17 km from the summit craters, at an elevation of 560 m a.s.l.), Tremestieri Etneo (T; 21 km and 350 m a.s.l.), and Rifugio Citelli (C; 6 km and 1740 m a.s.l.) (Fig. 3). The camera orientations were selected to record volcanic activity while complying with privacy regulations. In September 2025, positions A and T were updated to the current configuration for long-term monitoring networks (Sect. 2.1), while position C was dismissed following the unavailability of power supply to run the camera nodes. For the Mt. Etna network, the nominal sampling interval during daytime is 3 s. While sampling interval is progressively increased during twilight and night to observe eventual ash emissions, a low frequency visible acquisition (one image per hour) is retained overnight to document eventual lava flows. Data transfer to a remote server is managed autonomously.

2.3.2 Geneva Jet d'eau (Switzerland)

To validate the temporary network configuration in a controlled and easily accessible setting, we deployed three camera nodes at the Geneva Jet d'eau (Switzerland) in May 2025. The Jet d'eau is a high contrast, vertical water fountain with quasi constant height located in Lake Geneva (Fig. 4a). According to the Services Industriels de Genève (SIG), the Jet d'eau reaches a maximum height of 140 m, with a projection velocity of 200 $\mathrm{km\,h^{-1}}$ and a flow rate of 500 $\mathrm{L\,s^{-1}}$. These stable and documented characteristics make it suitable for testing acquisition stability, image quality, and the post-processing pipeline used for height measurements. During the test, the nodes were operated in video mode, with one camera node placed at the southeast (J, recording at 1080p50) and two camera nodes at the southwest (G, recording at 1080p50 and 480p120, respectively) of the nozzle (Fig. 4a). These two locations were chosen to simulate a field deployment under wind conditions that can bend plume-shaped objects. In addition, a reference recording was acquired with an independent consumer camera (Canon Legria HF G50, recording at 1080p50) from the southwestern location, to benchmark the derived height time series.

2.3.3 Stromboli (Italy)

The temporary configuration was also used in September 2025 as a support imaging system during a field campaign at Stromboli (Italy). The main objective was to obtain a visual record of eruptive activity to complement aircraft based measurements (e.g., Thivet et al., 2025, 2026). The camera node was primarily installed at Punta Labronzo (L, at 1.9 km from the summit craters, at an elevation of 110 m a.s.l.; Fig. 4b) and operated in still image timelapse mode with a nominal sampling interval of 3 s. The node was operated in a standalone mode with local storage and periodic USB or `scp` data transfer.

For one day, the system was deployed at Pizzo (P, at 0.25 km from the summit craters, at an elevation of 915 m a.s.l.; Fig. 4b), together with another camera node simultaneously dedicated to supporting a volcanic ash electrical charge and settling velocity measurement device (VoltAsh-Pi; Fries et al., 2026b). This node used specific video recording settings (1500×700 pixels, a focal distance of 12.5 cm, at 120 fps) to image particle fallout.

https://doi.org/10.5194/egusphere-2026-4353
Preprint. Discussion started: 11 August 2026

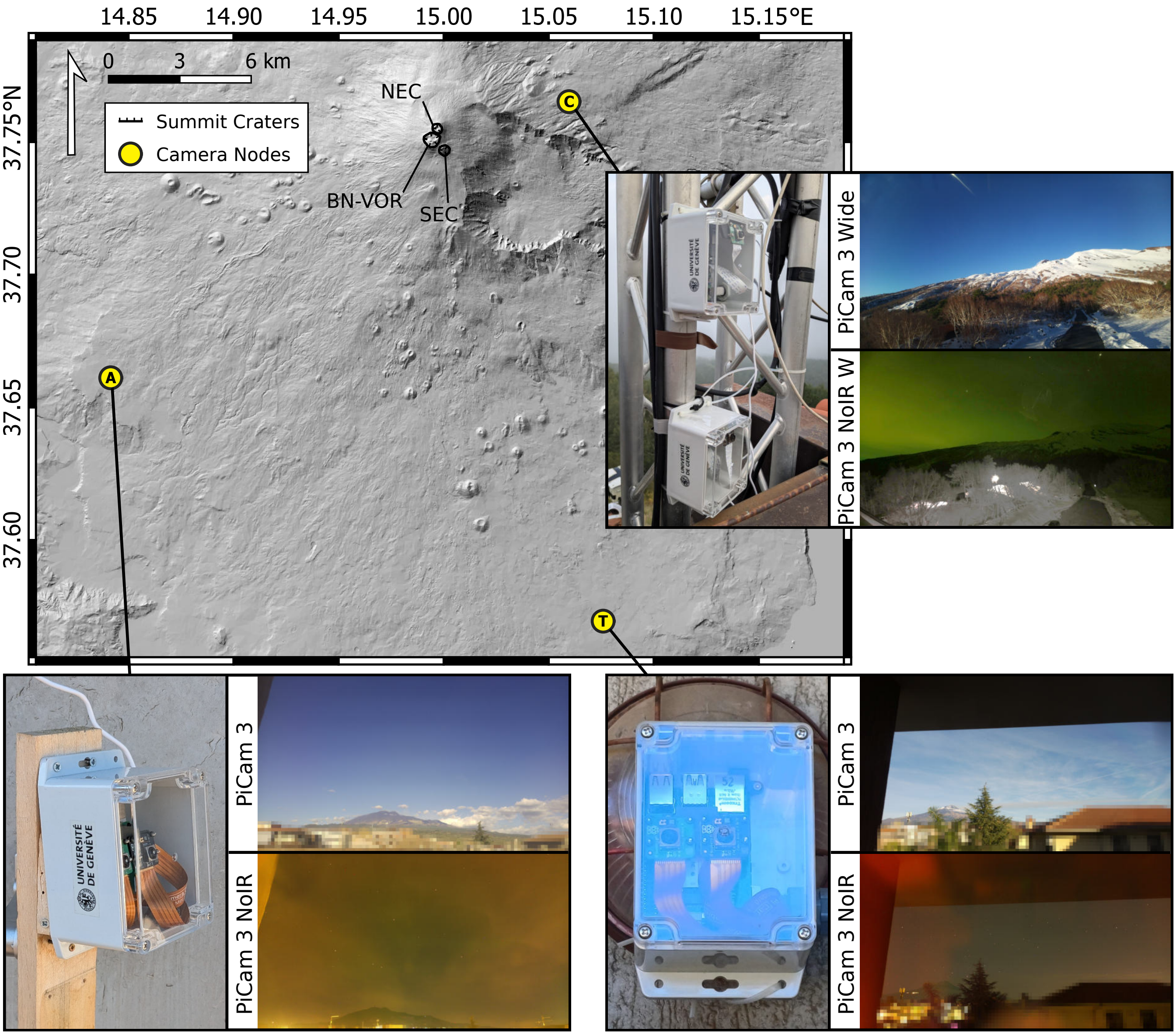

Figure 3. Location of the three installation sites for the permanent network at Mt. Etna (Italy) with respect to the summit craters (BN, Bocca Nuova; NEC, North-East Crater; SEC, South-East Crater; V, Voragine;): Adrano (A), Tremestieri Etneo (T), and Rifugio Citelli (C). For each location, the insets show a picture of the camera nodes as installed and an example of the two types of images that are recorded (i.e., during day- and nighttime). Sensitive areas in the foreground were anonymised through pixelation. Basemap from TINITALY/1.1 DEM (Tarquini et al., 2023).

https://doi.org/10.5194/egusphere-2026-4353
Preprint. Discussion started: 11 August 2026

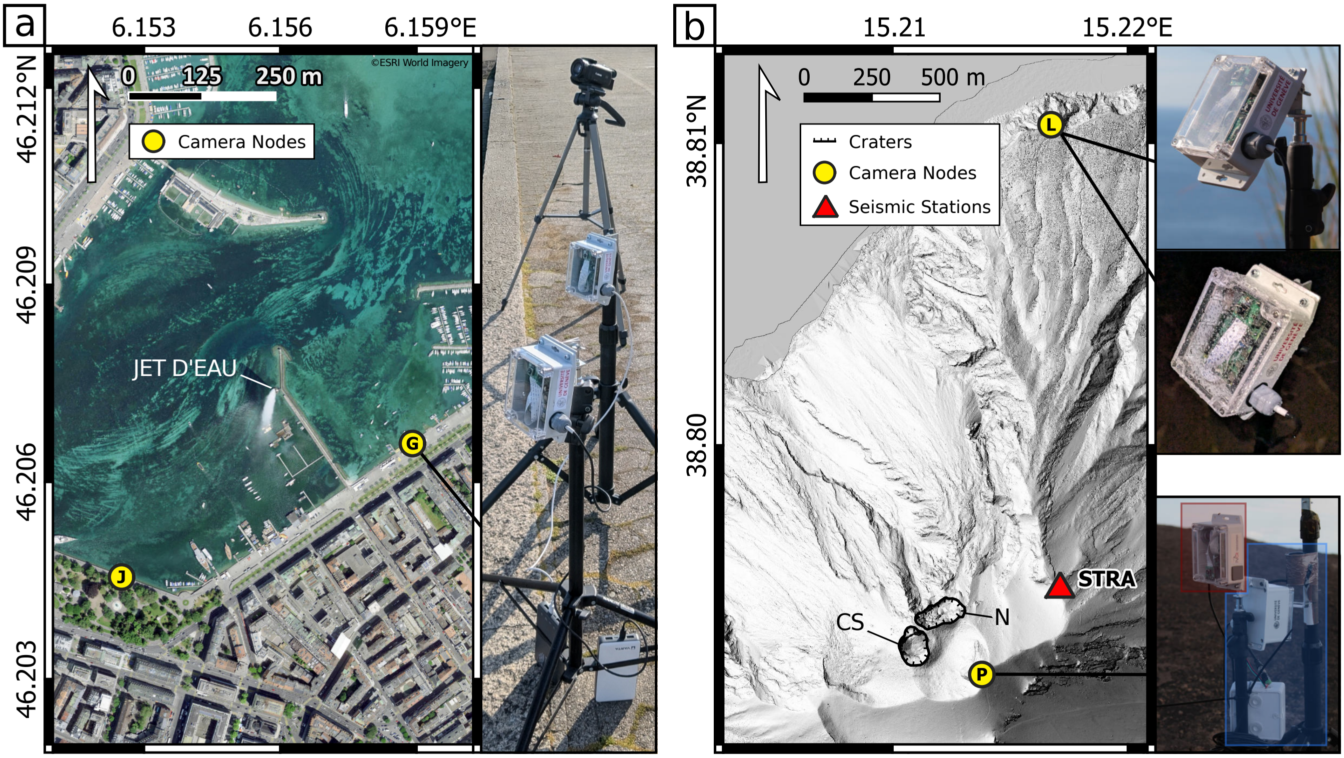

Figure 4. Camera locations for the temporary deployments at (a) the Geneva Jet d'eau (Switzerland) (satellite imagery from Esri | Powered by Esri) and (b) Stromboli (Italy) (DSM basemap from Bisson et al., 2023, and Civico et al., 2024). (a) At the Jet d'eau, one camera node was installed at the southeast (J; 1080p50) and two camera nodes at the southwest (G; 1080p50 and 480p120) of the nozzle; a colocated reference recording was acquired from the southwestern site with a Canon Legria HF G50 (1080p50). (b) At Stromboli, the node was primarily deployed at Punta Labronzo (L) and, for one day, at Pizzo (P), closer to the summit craters (N, North, and CS, Central South craters). The installation at site P (bottom image) consisted in a temporary camera node to image the CS crater (red box) and a second node to support a volcanic ash electrical charge and settling velocity measurement device (blue box).

2.3.4 Laboratory experiment

To test the same temporary configuration outside field conditions, we also used a camera node during a controlled laboratory experiment. The objective was not to reproduce a natural eruption, but to verify whether the acquisition workflow could capture and rapidly process short duration, high speed image sequences. A buoyant plume was generated by injecting water at $20.7\ ^{\circ}\mathrm{C}$, with a sugar concentration of $0\ \mathrm{g\,L^{-1}}$ and a density of $997.4\ \mathrm{kg\,m^{-3}}$, into a denser ambient sugar solution at $21.2\ ^{\circ}\mathrm{C}$, with a sugar concentration of $132.5\ \mathrm{g\,L^{-1}}$ and a density of $1048.5\ \mathrm{kg\,m^{-3}}$. This density contrast corresponds to a reduced gravity (i.e., the effective buoyancy acceleration due to the density difference) of approximately $0.48\ \mathrm{m\,s^{-2}}$. The camera node recorded the experiment at $120\ \mathrm{fps}$, and the sequence was then processed frame by frame to track the plume front and retrieve a time series of plume height and ascent velocity.

https://doi.org/10.5194/egusphere-2026-4353
Preprint. Discussion started: 11 August 2026

2.4 Post processing of obtained data

For lava flow front tracking at Mt. Etna, we use a geometric projection approach based on ray–terrain intersection. Let (i,j) denote a pixel coordinate in an image of size $W \times H$, and let β_H and β_V denote the horizontal and vertical field of view. Pixel coordinates are horizontally and vertically mapped to angular offsets from the optical axis as

$$\theta_H(i) = -\frac{\beta_H}{2} + \left(i + \frac{1}{2}\right)\frac{\beta_H}{W}, \qquad \theta_V(j) = -\frac{\beta_V}{2} + \left(H - j + \frac{1}{2}\right)\frac{\beta_V}{H}. \tag{1}$$

We then account for camera orientation in the map reference frame. Here, φ is the camera pitch (inclination from horizontal), κ is the camera roll (image plane rotation), and ω is the camera azimuth (heading, i.e., viewing direction in the horizontal plane). The corresponding rotation matrices are

$$\mathbf{R}_y(\kappa) = \begin{bmatrix} \cos\kappa & 0 & -\sin\kappa \\ 0 & 1 & 0 \\ \sin\kappa & 0 & \cos\kappa \end{bmatrix}, \qquad \mathbf{R}_z(\omega) = \begin{bmatrix} \cos\omega & -\sin\omega & 0 \\ \sin\omega & \cos\omega & 0 \\ 0 & 0 & 1 \end{bmatrix}. \tag{2}$$

The unit ray direction in the map reference frame is obtained as

$$\mathbf{d}_w(i,j) = \mathbf{R}_z(\omega)\,\mathbf{R}_y(\kappa)\,\mathbf{d}_c(i,j), \tag{3}$$

where the unit viewing direction in the camera frame is

$$\mathbf{d}_c(i,j) = \begin{bmatrix} \cos(\varphi + \theta_V)\sin\theta_H \\ \cos(\varphi + \theta_V)\cos\theta_H \\ \sin(\varphi + \theta_V) \end{bmatrix}. \tag{4}$$

By construction, $\mathbf{d}_c$ (and thus $\mathbf{d}_w$) is a unit vector (i.e., $\|\mathbf{d}\| = 1$). This normalisation ensures that the ray parameter s has the physical meaning of distance along the line of sight (in metres), so that $s\,\mathbf{d}_w$ is a displacement of length s. For a camera position $\mathbf{p}_0 = (x_0, y_0, z_0)$, the corresponding 3D ray is

$$\mathbf{p}(s) = \mathbf{p}_0 + s\,\mathbf{d}_w, \qquad s \geq 0. \tag{5}$$

We sample s along the ray up to a maximum distance and compare the ray elevation $z(s)$ with a digital elevation model (DEM) height $z_{\mathrm{DEM}}(x(s), y(s))$ at the projected coordinates. The first crossing $z(s) < z_{\mathrm{DEM}}$ is interpreted as the terrain intersection, and the corresponding elevation is assigned to pixel (i,j), yielding a per pixel projected-elevation (contour) image. A sub step linear interpolation between the last two samples provides a refined estimate of the intersection point. This projected-elevation matrix is then used to extract the corresponding elevation from the matrix to build a time series of lava front altitude by manually picking the lava front location in the camera image (pixel coordinates). For this purpose, we used a 10 m resolution TINITALY/1.1 DEM (Tarquini et al., 2023).

Image based observations at Stromboli were compared with seismic data from the STRA seismic station situated at approximately 250 m from the summit craters (Fig. 4b). The waveform was corrected for the instrumental response. The spectrogram

https://doi.org/10.5194/egusphere-2026-4353
Preprint. Discussion started: 11 August 2026

is computed using the vertical component (HHZ) by applying a 1–20 Hz band pass filter, and converting the signal to ground velocity.

Quantitative measurements of plume-shaped objects from visible imagery, presented as application of the camera nodes in this paper, are obtained with the PlumeTraP workflow (Simionato et al., 2022), which detects and parametrises the target to produce time series such as height, width, and derived kinematics. PlumeTraP applies a wind correction based on the method of Snee et al. (2023) using, for our applications, ERA5 (ECMWF Reanalysis v5) hourly data on pressure levels (Hersbach et al., 2023). When background, illumination, or atmospheric conditions are critical for the automatic detection of the target, a manual picking of the plume top is performed to obtain a height time series (Simionato et al., 2024).

3 Results

3.1 Long-term monitoring network

The Mt. Etna environment, even though located relatively close to several towns and only 30–35 km from Catania, presents variable and sometimes severe meteorological conditions, including snow, rain, ash fallout, and extreme temperatures. For example, between September 2024 and September 2025, temperatures recorded by meteorological stations close to our installation sites ranged from $-5.8\,^{\circ}\mathrm{C}$ (site C, December 2024) to $43\,^{\circ}\mathrm{C}$ (site A, July 2025). After one year of testing under these conditions, only two camera nodes stopped working due to OS corruption (caused by the long-term use of microSD memory cards for storage). This led to the aforementioned hardware update for long-term monitoring networks (Sect. 2.3, detailed in Sect. 2.1), implemented to reduce the risk of storage corruption caused by unexpected power failures during write operations or excessive write cycles. Once the network was updated to the latest configuration, the main disruptions to the data stream were related to the Wi-Fi connectivity of the private houses hosting the camera nodes. Otherwise, the cameras have operated without on site intervention since then.

3.1.1 Application to February 2025 Mt. Etna activity

Based on observations from the camera network, during February 2025, Mt. Etna exhibited a sustained eruptive phase marked by the coexistence of effusive and moderate explosive activity (Fig. 5a). The first recorded activity occurred on the night of 6 February 2025, with intermittent Strombolian explosions originating from the area of the South-East Crater (SEC). Two days later, on the evening of 8 February 2025, the activity evolved into an effusive phase triggered by the opening of a fissure at the base of the Bocca Nuova (BN) crater, situated at approximately 3000 m a.s.l. (Fig. 5). The following morning, the active front of the lava flow already reached an altitude of approximately 2800 m a.s.l. Lava flows propagated rapidly toward the southwest, moving across snow covered terrain, and descended to an altitude of approximately 2000 m a.s.l. on 12 February 2025 (Fig. 5b–c). Between 12 and 17 February 2025, explosive activity intensified, with ash emissions forming low altitude columns (Fig. 5a, black contoured bottom images), while the active lava flow front reached an altitude of approximately 1800 m a.s.l. Following a temporary decline in activity, including reduced lava output and the cessation of explosions at the SEC, activity resumed

https://doi.org/10.5194/egusphere-2026-4353
Preprint. Discussion started: 11 August 2026

on 21 February 2025, with a new pulse of lava effusion and, from 23 February 2025, strong degassing and/or low intensity ash emissions. This new lava emission from the same fissure at the base of BN generated a new branch slightly shifted to the southern side of the flank, reaching an altitude of approximately 2700 m a.s.l. on the morning of 22 February 2025 and merging with the older branch the following day. The activity persisted until 25 February 2025, when the lava flow reached an altitude of approximately 2250 m a.s.l. and both explosive intensity and effusion rates decreased again. Activity increased again on 27 February 2025, marked by renewed lava emission from the same fissure (a new southernmost branch formed) and sporadic Strombolian explosions at the SEC. This episode lasted until 2 March 2025, when an active lava flow was last observed and a final altitude for this branch was reached at approximately 2500 m a.s.l.

3.2 Temporary installations

The temporary configuration was tested at the Geneva Jet d'eau and subsequently used during a field campaign at Stromboli, covering both high frame rate video acquisition (1080p50 and 480p120) and still image timelapse acquisition at a nominal sampling interval of 3 s. During these deployments, the system operated in standalone mode under day- and nighttime conditions, as well as during heavy rain (Fig. 4b). Power supplied by 20000 mAh power banks was sufficient to run the system for at least 20–24 h, depending on acquisition mode.

3.2.1 Validation of the system at the Geneva Jet d'eau

We validated the temporary deployment configuration at the Geneva Jet d'eau by analysing colocated recordings acquired at the southwestern site with a Raspberry Pi camera node and a Canon Legria G50 reference camera (Fig. 4a). For each instrument, we extracted a 5-min height time series at 1 Hz (300 frames) and computed jet height above the nozzle level. In addition, we processed short 4.5 s video sequences acquired at 1080p50 and 480p120 to assess the behaviour of the workflow at higher temporal resolution (Fig. 6).

For the 5-min sequences, the Raspberry Pi time series yields a mean jet height of 121.5 m above the nozzle (maximum 130.1 m), while the Canon reference yields a mean of 118.8 m (maximum 127.5 m). The agreement between the two time series is good, with a median relative difference of 1.8 % (95th percentile 4.0 %; mean 2.4 %), computed pointwise relative to the Canon reference.

At high frame rates (50–120 fps), height estimates remain consistent but become increasingly sensitive to pixel level tracking noise, especially at 120 fps. After resampling the 120 fps series to the 50 fps timestamps, the median relative difference is 1.7 % (95th percentile 3.7 %; mean 1.7 %). At the Jet d'eau viewing distance, the mean projected pixel size is on the order of $0.18\ \mathrm{m\,px^{-1}}$ at 1080p50 and $0.29\ \mathrm{m\,px^{-1}}$ at 480p120. This difference is small compared to other sources of uncertainty, therefore, having a lower spatial resolution does not significantly affect the retrieved height at this distance (275 m). Overall, for this validation target, 50 fps already captures the relevant height variability, whereas 120 fps primarily increases noise in time derivative quantities (velocity and acceleration) without providing additional insight for the height retrieval.

https://doi.org/10.5194/egusphere-2026-4353
Preprint. Discussion started: 11 August 2026

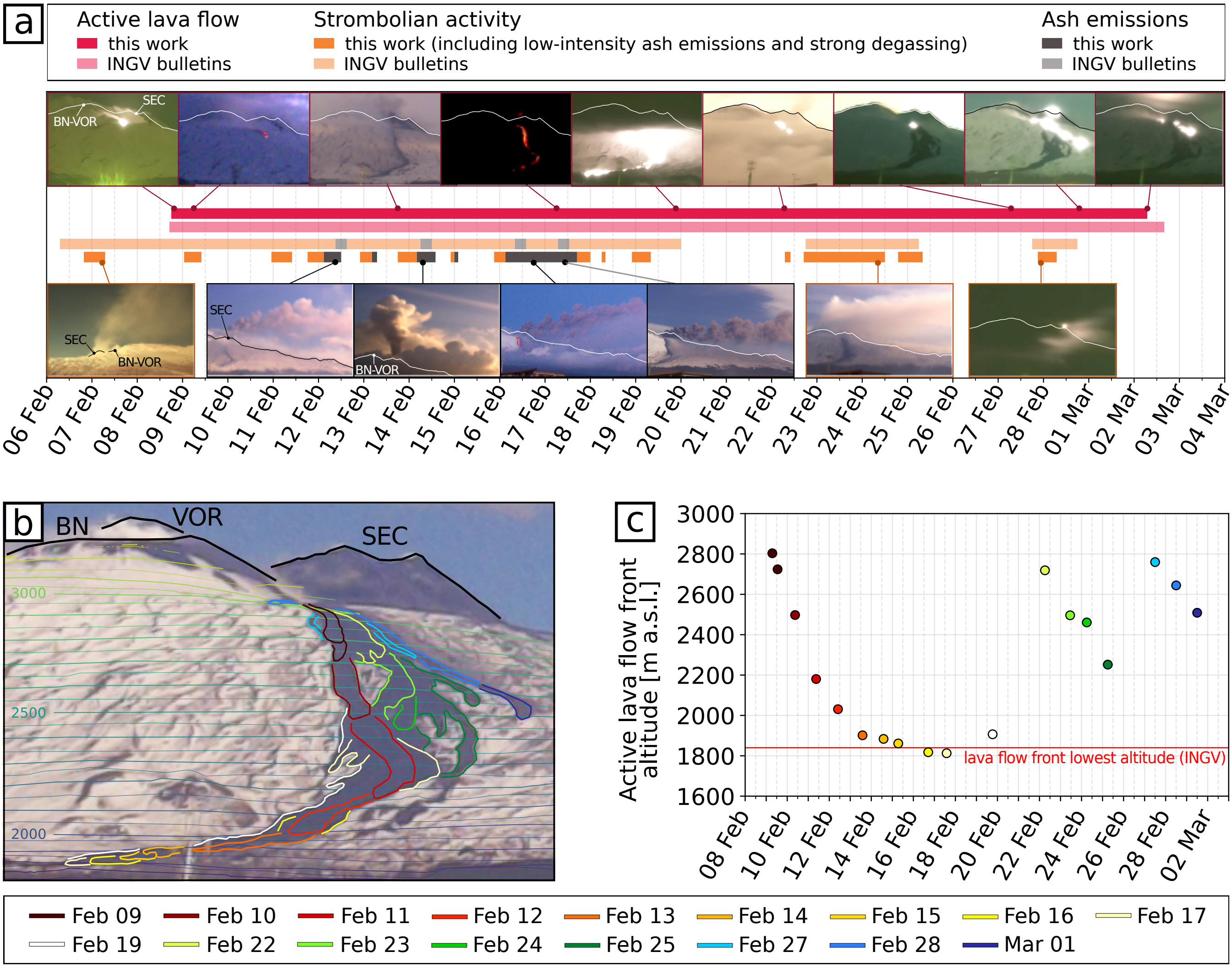

Figure 5. (a) Timeline of Mt. Etna activity from 6 February to 3 March 2025 (UTC+1), based on observations from the camera network (darker tones) and INGV (Istituto Nazionale di Geofisica e Vulcanologia) bulletins (lighter tones). Coloured bars indicate time spans for active lava flow (red), ash emissions (grey), and Strombolian activity (orange; including low intensity ash emissions or strong degassing in our observations). Example images from the long-term monitoring network (stations A and C) are shown, with the position of Bocca Nuova (BN), Voragine (VOR), and South East Crater (SEC) indicated. (b) Lava flow evolution and (c) altitude a.s.l. of the active lava flow front, retrieved from camera imagery using DEM projection onto the image plane (height isolines are superimposed on the Mt. Etna profile). Different colours represent different days in the period from 8 February to 2 March 2025. The lowest active front altitude reported by INGV is also shown (solid red line).

https://doi.org/10.5194/egusphere-2026-4353
Preprint. Discussion started: 11 August 2026

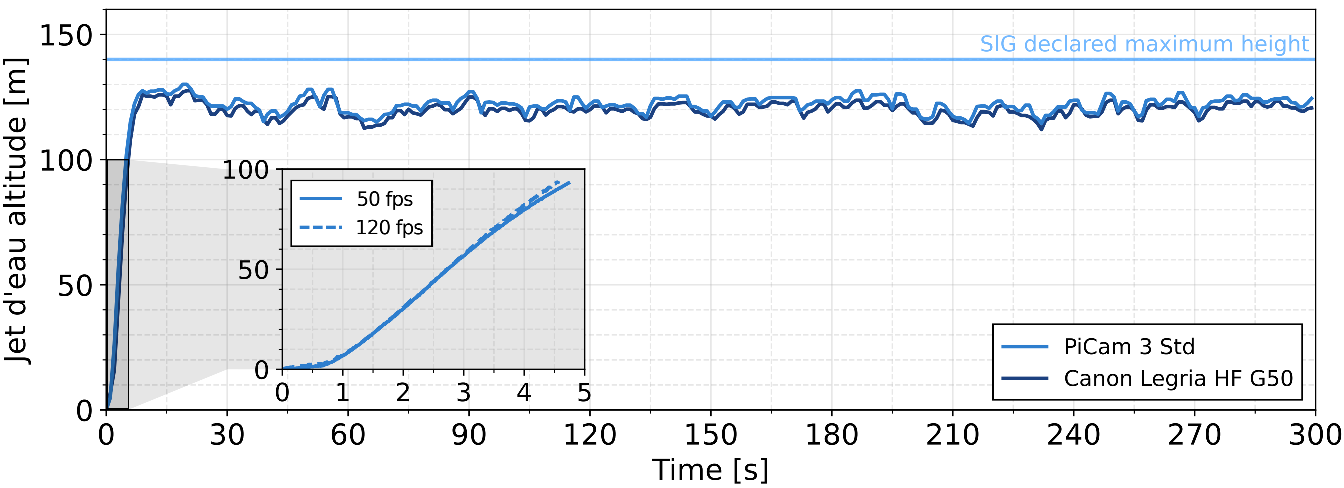

Figure 6. Jet d'eau altitude above nozzle level measured from image analysis of videos recorded at 1080p50, resampled at 1 Hz, with our camera nodes (light blue) and with a Canon Legria HF G50 (dark blue). The nominal maximum height declared by SIG (Services Industriels de Genève) is shown (light blue horizontal line). The inset shows measurements for the first 4.5 s at 1080p50 (solid line) and 480p120 (dashed line).

3.2.2 Application to September 2025 Stromboli activity

During the September 2025 Stromboli field campaign, the temporary camera node provided a robust visual record of explosive activity and associated ash emissions over multiple days (Fig. 7a). Across six recording windows totalling 22.7 h, we recognised 106 ash plume events, corresponding to an average rate of 4.68 events per hour of recording. The number of events varied substantially between days, with 4 events on 20 September 2025, 9 on 21 September 2025, 6 on 22 September 2025, 28 on 23 September 2025, 42 on 24 September 2025, and 17 on 26 September 2025 (Fig. 7a). These observations demonstrate that, even in a standalone configuration, the node can deliver continuous, timestamped imagery suitable for both qualitative and quantitative analysis of volcanic activity.

We further analysed in detail a subset of eight ash plumes on 23 September 2025 between 11:34 and 12:57 (UTC+2), for which top tracking could be performed consistently (Fig. 7c). Retrieved maximum plume heights range from 1050 to 1525 m a.s.l., with a mean height uncertainty of $\sim$ 20–26 m.

3.2.3 Support to laboratory experiments

In addition to field deployments, the system can be used in other settings, including as a support to controlled laboratory experiments. Here, we tested high speed image acquisition and rapid quantitative post-processing on a transient experimental plume. The resulting image sequence was used to retrieve plume front displacement through time, while the instantaneous velocity was computed as the numerical time derivative of this series. Over the analysed 0.525 s window, the plume height increased up to 7.18 cm. The mean ascent velocity over the interval was 13.68 $\mathrm{cm\,s^{-1}}$, with peak instantaneous velocities

https://doi.org/10.5194/egusphere-2026-4353
Preprint. Discussion started: 11 August 2026

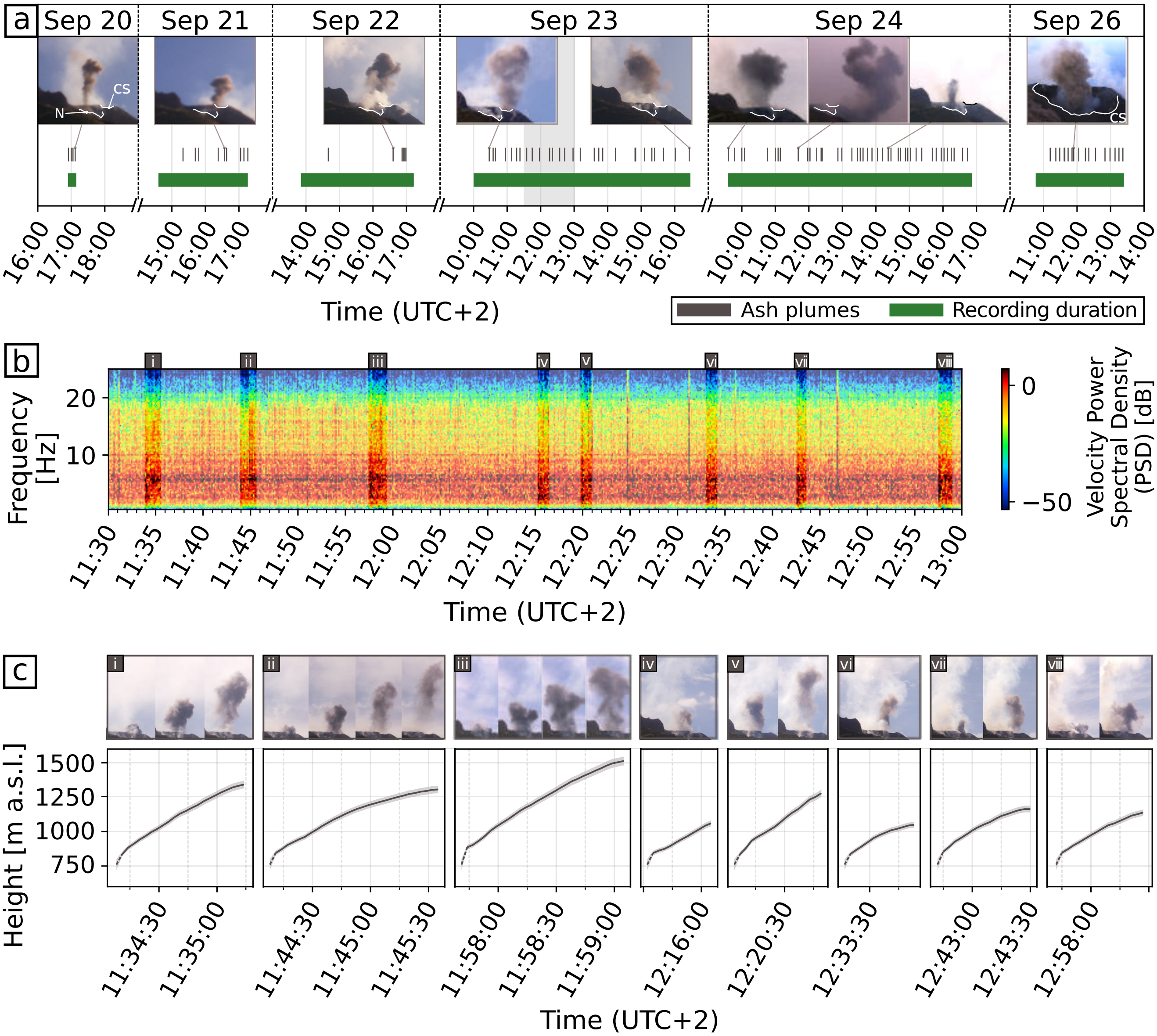

Figure 7. (a) Timeline of Stromboli ash emissions (grey bars) from 20 to 26 September 2025, based on observations from the camera node (green bars show the recording duration), with example images, in which the position of North (N) and Central South (CS) craters are indicated. The grey shaded area identifies the period between 11:30 and 13:00 (UTC+2) on 23 September 2025, during which eight events (i–viii) are analysed in detail in (b) and (c). (b) Seismic spectrogram of the vertical component (HHZ) recorded at station STRA. Intervals from 15 s before each first observed ash plume image to the end of each event are shown at full opacity. (c) Ash plume heights (solid lines) as a function of time, with example images of plume evolution. Shaded areas indicate uncertainty from geometric parameters, and dashed lines indicate the uncertainty on the initial plume rise phase that is obscured by the crater rim.

https://doi.org/10.5194/egusphere-2026-4353
Preprint. Discussion started: 11 August 2026

reaching approximately $100\,\mathrm{cm\,s^{-1}}$ during the initial rise phase (Fig. 8). These results illustrate the capability of the system to capture short duration experiments at high frame rate.

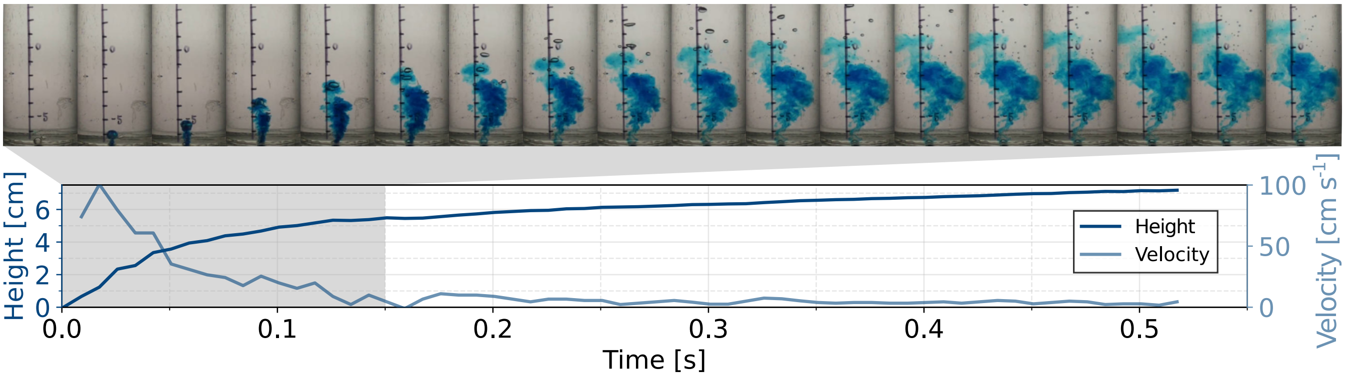

Figure 8. Laboratory plume experiment recorded at 120 fps (top row shows the first 18 frames of the sequence, for a total duration of 0.15 s). The plume height (dark blue) is derived from frame by frame tracking, and the corresponding instantaneous ascent velocity (light blue) is computed from the time derivative of the height series.

4 Discussion

300 ### 4.1 Operational capabilities and limitations

The proposed system combines low cost hardware with lightweight automation to support both long-term deployments and rapid, temporary installations. Durability and trustworthiness over extended periods are fundamental for long-term monitoring networks, as access to installation sites may be restricted or difficult. In contrast to predefined proprietary webcam systems or commercial video cameras, the acquisition framework is fully customisable (e.g., capture interval, resolution, exposure, illumination-dependent scheduling, transfer logic), enabling end users to tailor the system to site specific constraints and scientific objectives (cf. Simionato, 2026). In the long-term configuration, autonomous scheduling, systematic folder organisation, and periodic health checks enable unattended operation over long periods, while keeping the workflow transparent, reproducible, and adaptable to specific needs. In temporary deployments, the same acquisition chain can be used in a standalone mode, where the key requirement is to maintain reliable timestamped imagery during predefined observation windows. Both installation types were exposed to variable and sometimes severe meteorological conditions, including snow, rain, ash fallout, and extreme temperatures (with reported values ranging from $-5.8\,^{\circ}\mathrm{C}$ to $43\,^{\circ}\mathrm{C}$ at stations close to the sites). Under these conditions, the nodes operated without on site intervention, supported by the sealed enclosure and the watchdog-based self recovery logic.

Across the different use cases presented here (field campaigns, near real time monitoring, and laboratory experiments), the system provides robust acquisition and local data management, complemented by optional real time transfer for remote

https://doi.org/10.5194/egusphere-2026-4353
Preprint. Discussion started: 11 August 2026

monitoring and downstream processing. This might allow near real time post-processing that converts image measurements into physically meaningful time series (e.g., plume height, lava front elevation) that can support volcano observatories and research. Such image streams could also be coupled with automated image analysis workflows for volcanic plumes, for example to improve segmentation quality and reduce processing time during plume detection and tracking (e.g., D'Adamo et al., 2026). From an operational perspective, the system is designed to be compatible with typical observatory constraints, where networks may need to be expanded quickly, maintained with limited field access, and operated under heterogeneous site conditions. The low cost and modular architecture supports instrument redundancy, while the minimal software stack and scheduling facilitates standardised configuration across stations. Optional near real time transfer and watchdog-based recovery enable rapid visual verification and early detection of failures, while still allowing offline operation when connectivity is intermittent. As a result, the approach can complement existing observatory monitoring infrastructures by providing high frequency data streams that are straightforward to archive, distribute, and post process. Temporary deployments may cover specific locations during crises (e.g., new fissures or flank eruptions) or dedicated campaigns. More generally, keeping the acquisition and transfer logic in a small set of open and editable scripts can also facilitate reproducibility and adaptation to existing observatory pipelines.

The main operational constraints identified during field use relate to power management and connectivity. Continuous acquisition and transfer are constrained by available power and network reliability. When grid power is unavailable at remote sites, either configuration can be powered by external batteries. While both power banks and batteries are ultimately energy storage, power banks offer convenient $5\ \mathrm{V}$ plug and play operation for short campaigns, whereas $12\ \mathrm{V}$ lead acid or lithium iron phosphate ($LiFePO_4$) batteries scale better to multi day autonomy (especially when paired with solar charging) at the cost of additional power electronics (DC–DC conversion and battery management) and increased weight. As an order of magnitude estimate, a $20000\ \mathrm{mAh}$ power bank (nominally $\sim 74\ \mathrm{Wh}$ at cell voltage) provides on the order of 10–$15\ \mathrm{h}$ of autonomy for a node drawing 6–8 W continuously, depending on hardware and operating mode; for a temporary configuration acquiring images at $0.33\ \mathrm{Hz}$, autonomy can reach 20–$24\ \mathrm{h}$. A $12\ \mathrm{V}$, $60\ \mathrm{Ah}$ battery stores $\sim 720\ \mathrm{Wh}$ nominal, corresponding to roughly 1.5–$3\ \mathrm{d}$ of autonomy for lead acid (typical depth of discharge constraints) and up to ~ 3–$4\ \mathrm{d}$ for $LiFePO_4$, depending on conversion losses and battery management. Regarding connectivity, the framework can operate in remote areas by relying on a local IP (Internet Protocol) network, e.g., wired local area network (LAN), Wi-Fi, or cellular links via SIM based USB/Long-term Evolution (LTE) dongles. These transfer methods do not necessarily require public Internet access, as they can operate within private networks as long as the node and the receiving server are reachable via IP. Field logistics are therefore an important practical advantage of the proposed approach, as a camera node relying on power banks and cellular connectivity can be deployed and become operational after boot, without requiring additional on site interaction. A battery powered, cellular transfer configuration of the camera system is currently being implemented at Nyiragongo volcano (Democratic Republic of the Congo), where autonomous systems are particularly relevant for remote deployments. Moreover, two practical aspects for network operation deserve explicit consideration. First, high frequency imagery can rapidly generate large data volumes. Adaptive sampling (illumination-dependent intervals, event triggered acquisition), compression, and local buffering with staged transfer are therefore important to keep storage and bandwidth requirements manageable. Second, quantitative time series rely on accurate timestamps when measurements are compared across stations or with other sensors. This is generally ensured by

https://doi.org/10.5194/egusphere-2026-4353
Preprint. Discussion started: 11 August 2026

time synchronisation with NTP (Network Time Protocol) servers when the node has network access, otherwise it should be handled manually or by using an external real time clock (RTC) module, especially after reboots or long offline periods. For harsh environments (e.g., proximal crater areas), robust protective cases (e.g., Pelican type) and protective windows (glass or polycarbonate) can reduce the risk of damage from tephra and wind driven debris.

4.2 Case studies and validation

In this paper, we evaluated the proposed framework through long-term monitoring network observations and DEM-based lava front tracking at Mt. Etna, a controlled validation of a temporary configuration against a reference camera at the Geneva Jet d'eau, and temporary field and laboratory deployments aimed at plume height and/or kinematics retrieval.

At Mt. Etna, the long-term monitoring network provided a record of the February 2025 activity and enabled tracking of lava flow front altitude through time. The events described from the visual observation of the image time series (Sect. 3.1.1) show a general correspondence with the description of the activity from INGV bulletins (Fig. 5a; INGV, 2025a, b, c, d, e). The active lava flow was documented throughout the period in the images from the camera network, while Strombolian activity and ash emissions were sometimes not detected due to relatively low altitude atmospheric clouds. The retrieved front altitudes of the active lava flow and their temporal evolution are consistent with satellite imagery presented by Ganci et al. (2025), while offering a much denser temporal sampling than is typically achievable with satellite imagery alone, typically limited by revisit time and atmospheric constraints. Indeed, even if we presented one measurement per day (Fig. 5b-c), the temporal resolution might be drastically increased for several days during February 2025 activity. However, these DEM-based projections can be highly influenced by the geometric uncertainty linked to camera calibration (location, orientation, and optics) and DEM resolution, while the discretisation of the ray projection step adds an additional, usually smaller, resolution-limited contribution. Therefore, an accurate calibration is necessary before retrieving quantitative data, also considering that the picking of the front position, which may be affected by haze, water vapour, or low contrast, may also introduce subjective errors.

For the Geneva Jet d'eau benchmark, the comparison between the camera node and the commercial reference shows that the system can reproduce the main height variability, with differences that are small relative to the typical amplitude of the signal. In both our measurements, the retrieved jet heights remain below the nominal maximum height reported by SIG. This reference value is not provided as a synchronous measurement and likely reflects a different definition or operating conditions (e.g., a maximum under specific pump settings and wind conditions, averaged or representative over longer time spans) rather than a systematic bias in the two camera based retrievals. In this example, the sensitivity of derived quantities to acquisition settings becomes evident. While the height time series remains robust, higher frame rates (e.g., 480p120) increase sensitivity to pixel scale tracking noise and, therefore, could amplify scatter in time derivative estimates (velocity and acceleration).

At Stromboli, the temporary configuration demonstrated that a standalone node can deliver continuous, timestamped imagery suitable for both qualitative assessment and quantitative plume top tracking during a field campaign, including under adverse meteorological conditions and also as support to other instrumentation. The simultaneous seismic spectrogram shows that the eight ash plume events selected from the camera imagery correspond to low frequency seismic signals, supporting their identification as explosive events. Additional high amplitude seismic signals are also visible in the same time window but

https://doi.org/10.5194/egusphere-2026-4353
Preprint. Discussion started: 11 August 2026

were not associated with ash plumes in the analysed images. These may correspond to other types of activity, such as ballistic rich explosions, gas thrust events, rockfalls, or debris avalanches, illustrating the complementarity between visual and seismic observations.

Finally, the laboratory plume experiment illustrates that the same hardware and software stack can be used outside of volcano monitoring, providing high speed acquisition, in this case not limited by pixel size, as the distance from the target is largely reduced.

5 Conclusions

This study presents an open source, cost-effective framework for visible wavelength camera nodes and networks, aimed at continuous volcano monitoring as well as rapid deployment during field campaigns and experiments, or as support to other instruments. By combining consumer grade imaging hardware with a lightweight and fully customisable acquisition stack, the system enables flexible configuration of sampling strategy, illumination-dependent settings, local archiving, optional transfer, and basic self recovery. This design allows end users to adapt operation to site constraints (power, connectivity, weather exposure) while maintaining transparent and reproducible workflows. The first deployments demonstrate the reliability and flexibility of the system for different acquisition needs. Long-term observations at Mt. Etna allowed us to document explosive activity at the summit craters and to measure the progression of lava flows during the February–March 2025 eruption. After validation against a reference camera at the Geneva Jet d'eau, short-term deployments at Stromboli showed that the temporary configuration can be used to visualise volcanic ash plumes and track their height evolution, while the laboratory experiment demonstrated its usefulness for controlled high speed imaging.

More generally, such camera nodes can complement existing observatory infrastructures by providing high frequency image time series that support both qualitative interpretation and quantitative measurements. Their possible use is not limited to the direct observation of volcanic craters, lakes, edifices, or plumes. Camera networks can also help document the state of roads, buildings, and other infrastructures during volcanic crises, providing rapid visual information that may improve response time during natural hazards. Broader deployment of such systems could also help build larger and more diverse image datasets across a wider range of volcanoes, including poorly monitored systems. This would support future artificial intelligence and machine learning applications while improving observational knowledge at sites where continuous visual records are still scarce. Beyond the case studies presented here, the same approach can be extended to any other targets where persistent or high temporal resolution imaging is needed, including applications across the natural sciences where camera networks provide basic observational data.

Code and data availability. The camera node software, setup scripts, and documentation are available at Simionato (2026). Images and/or videos analysed to generate datasets presented in this study, and additional scripts used for post-processing, are available at Simionato et al. (2026) and described in Supplements (Tables S1-S16), where datasets used to generate plots are also presented. Seismic data are part of the

https://doi.org/10.5194/egusphere-2026-4353
Preprint. Discussion started: 11 August 2026

INGV seismic network and are publicly available through EIDA Italia (eida.ingv.it, CC BY 4.0). The PlumeTraP software is available at Simionato (2024). Figures were generated using QGIS 3.22 Białowieża, Python scripts (v3.11.9), PGF/TikZ, and Inkscape 1.3.

Author contributions. RS: conceptualization, methodology, software, investigation, data curation, validation, visualization, writing (original draft). AF: conceptualization, methodology, investigation, writing (review and editing). ST: investigation, validation, writing (review and editing). JL: investigation, writing (review and editing). CDV: investigation, writing (review and editing). FA: resources. SS: resources, writing (review and editing). CB: conceptualization, supervision, funding acquisition, writing (review and editing).

Competing interests. The authors declare that they have no competing interests.

Acknowledgements. This research was supported by the Swiss National Science Foundation (SNSF/FNS) grant #200020_204315/1 and by the Alliance Campus Rhodanien project "VolCloud-AI - Exploration avancée des panaches et nuages volcaniques : traitement d'images multi-échelle par intelligence artificielle". The authors thank: the FacLab for supporting the development of 3D printed resources; Daniele Pennisi, Catherine Lemercier, Boris Behncke, Sandro, Gabriella and Fulvia for their help in the field at Mt. Etna; Marco Pistolesi, Marija Voloschina, Alessandro Aiuppa, and Tina at Stromboli; and Services Industriels de Genève (SIG) and, in particular, Alissandre Perotti-Grondin for allowing measurements at the Geneva Jet d'Eau.

https://doi.org/10.5194/egusphere-2026-4353
Preprint. Discussion started: 11 August 2026

References

Abaya, W. F., Basa, J., Sy, M., Abad, A. C., and Dadios, E. P.: Low cost smart security camera with night vision capability using Raspberry Pi and OpenCV, in: 2014 International Conference on Humanoid, Nanotechnology, Information Technology, Communication and Control, Environment and Management (HNICEM), pp. 1–6, https://doi.org/10.1109/HNICEM.2014.7016253, 2014.

Andò, B., Baglio, S., Castorina, S., and Campisi, A.: Characterization of a Vision-Based Tool for the Investigation of Geometric Characteristics of Ground-Deposited Volcanic Ash, Sensors, 22, 9616, https://doi.org/10.3390/s22249616, 2022.

Anthony, R. E., Ringler, A. T., Wilson, D. C., and Wolin, E.: Do Low-Cost Seismographs Perform Well Enough for Your Network? An Overview of Laboratory Tests and Field Observations of the OSOP Raspberry Shake 4D, Seismological Research Letters, 90, 219–228, https://doi.org/10.1785/0220180251, 2018.

Arason, P., Petersen, G. N., and Bjornsson, H.: Observations of the altitude of the volcanic plume during the eruption of Eyjafjallajökull, April–May 2010, Earth System Science Data, 3, 9–17, https://doi.org/10.5194/essd-3-9-2011, 2011.

Aubry, T. J., Engwell, S. L., Bonadonna, C., Mastin, L. G., Carazzo, G., Van Eaton, A. R., Jessop, D. E., Grainger, R. G., Scollo, S., Taylor, I. A., Jellinek, A. M., Schmidt, A., Biass, S., and Gouhier, M.: New Insights Into the Relationship Between Mass Eruption Rate and Volcanic Column Height Based On the IVESPA Data Set, Geophysical Research Letters, 50, e2022GL102 633, https://doi.org/10.1029/2022GL102633, 2023.

Awadallah, S., Moure, D., and Torres-González, P.: An Internet of Things (IoT) Application on Volcano Monitoring, Sensors, 19, 4651, https://doi.org/10.3390/s19214651, 2019.

Barnie, T., Hjörvar, T., Titos, M., Sigursson, E. M., Pálsson, S. K., Bergsson, B., Ingvarsson, Þ., Pfeffer, M. A., Barsotti, S., Arason, P., Þorvaldsson, V. S., von Löwis of Menar, S., and Oddsson, B.: Volcanic plume height monitoring using calibrated web cameras at the Icelandic Meteorological Office: system overview and first application during the 2021 Fagradalsfjall eruption, Journal of Applied Volcanology, 12, 4, https://doi.org/10.1186/s13617-023-00130-9, 2023.

Bisson, M., Gianardi, R., Civico, R., Madonia, P., Ricci, T., and Spinetti, C.: Lidar-derived digital surface model of Stromboli island updated to August 2023, https://doi.org/10.13127/stromboli/airborne-lidar-2023, 2023.

Catalan, L., Araiz, M., Aranguren, P., Padilla, G. D., Hernandez, P. A., Perez, N. M., Garcia de la Noceda, C., Albert, J. F., and Astrain, D.: Prospects of Autonomous Volcanic Monitoring Stations: Experimental Investigation on Thermoelectric Generation from Fumaroles, Sensors, 20, 3547, https://doi.org/10.3390/s20123547, 2020.

Civico, R., Ricci, T., and Scarlato, P.: High-Resolution SfM Topography of Stromboli volcano (Italy), 14 July 2024, https://doi.org/10.5069/G9S75DJH, 2024.

Clarkson, R.: Volcanic Ash and Aviation – Rolls-Royce Position, https://old.wmo.int/aemp/sites/default/files/VA_Brief_Summary_Rolls_Royce.pdf, 2017.

Clive, M. A. T., Lawson, R. V., Lamb, O. D., Potter, S., Kilgour, G., Jarvis, P. A., Harrison, S., Scott, B., and Charlton, D.: Crowdsourcing human observations expands and enhances volcano monitoring records, Communications Earth & Environment, 5, 1–10, https://doi.org/10.1038/s43247-024-01747-3, 2024.

Coltelli, M., D'Aranno, P. J. V., De Bonis, R., Guerrero Tello, J. F., Marsella, M., Nardinocchi, C., Pecora, E., Proietti, C., Scifoni, S., Scutti, M., and Wahbeh, W.: The Use of Surveillance Cameras for the Rapid Mapping of Lava Flows: An Application to Mount Etna Volcano, Remote Sensing, 9, 192, https://doi.org/10.3390/rs9030192, 2017.

https://doi.org/10.5194/egusphere-2026-4353
Preprint. Discussion started: 11 August 2026

D'Adamo, T., Thivet, S., Pothier, C., Simionato, R., Fries, A., Lemus, J., Bonadonna, C., Tougne Rodet, L., and Keraudret, B.: GuidedSAM-Plume: An expert-guided segmentation framework for volcanic plumes, in: ICPR 2026 Workshop proceedings, accepted, 2026.

de Michele, M., Raucoules, D., and Arason, P.: Volcanic Plume Elevation Model and its velocity derived from Landsat 8, Remote Sensing of Environment, 176, 219–224, https://doi.org/10.1016/j.rse.2016.01.024, 2016.

Degruyter, W. and Bonadonna, C.: Improving on mass flow rate estimates of volcanic eruptions, Geophysical Research Letters, 39, https://doi.org/10.1029/2012GL052566, 2012.

Diaz, J., Cervone, G., and Wauthier, C.: Improving the Thermal Infrared Monitoring of Volcanoes: A Deep Learning Approach for Intermittent Image Series, https://doi.org/10.48550/arXiv.2109.12767, 2021.

Dürig, T., Gudmundsson, M. T., Dioguardi, F., Woodhouse, M., Björnsson, H., Barsotti, S., Witt, T., and Walter, T. R.: REFIR- A multi-parameter system for near real-time estimates of plume-height and mass eruption rate during explosive eruptions, Journal of Volcanology and Geothermal Research, 360, 61–83, https://doi.org/10.1016/J.JVOLGEORES.2018.07.003, 2018.

Fries, A., Lemus, J., Jarvis, P. A., Riccardo, S., Diaz-Vecino, C., B., C. A., C., P. J., Irene, M., and Costanza, B.: The temporal evolution of volcanic ash fingers and its effect on particle sedimentation, Journal of Geophysical Research: Solid Earth, in review, 2026a.

Fries, A., Rossi, E., Merrison, J. P., Iversen, J. J., Matsuyama, T., Arlaud, F., Lemus, J., Thivet, S., Carolina, D.-V., Simionato, R., and Bonadonna, C.: Measuring the electrical charge and settling velocity of volcanic ash particles with a new, cost-effective apparatus (VoltAsh) both in the laboratory and in the field, Bulletin of Volcanology, accepted, 2026b.

Ganci, G., Bilotta, G., Dozzo, M., Spina, F., Zuccarello, F., Cristofaro, R., Guardo, R., Spina, M., and Cappello, A.: Multi-platform satellite-derived products during the 2025 Etna eruption, Scientific Data, 12, 1353, https://doi.org/10.1038/s41597-025-05545-0, 2025.

Guffanti, M., Mayberry, G. C., Casadevall, T. J., and Wunderman, R.: Volcanic hazards to airports, Natural Hazards, 51, 287–302, https://doi.org/10.1007/S11069-008-9254-2/TABLES/3, 2009.

Guffanti, M., Casadevall, T. J., and Budding, K.: Encounters of Aircraft with Volcanic Ash Clouds: A Compilation of Known Incidents, 1953–2009, Tech. rep., https://pubs.usgs.gov/ds/545/, 2010.

Hersbach, H., Bell, B., Berrisford, P., Biavati, G., Horányi, A., Muñoz Sabater, J., Nicolas, J., Peubey, C., Radu, R., Rozum, I., Schepers, D., Simmons, A., Soci, C., Dee, D., and Thépaut, J.-N.: ERA5 hourly data on pressure levels from 1979 to present. Copernicus Climate Change Service (C3S) Climate Data Store (CDS)., https://doi.org/10.24381/cds.bd0915c6, 2023.

Hidayatullah, N. A., , Rakhmad Gusta, P., , Ardian Prima, A., , Dirvi Eko Juliando, S., , Kholis Nur, F., , Muhamad Fajar, S., , and Kalam, A.: Volcano multiparameter monitoring system based on Internet of Things (IoT), Australian Journal of Electrical and Electronics Engineering, 17, 228–238, https://doi.org/10.1080/1448837X.2020.1817250, 2020.

Horwell, C. J. and Baxter, P. J.: The respiratory health hazards of volcanic ash: a review for volcanic risk mitigation, Bulletin of Volcanology, 69, 1–24, https://doi.org/10.1007/s00445-006-0052-y, 2006.

Ilanko, T., Pering, T. D., Wilkes, T. C., Woitischek, J., D'Aleo, R., Aiuppa, A., McGonigle, A. J. S., Edmonds, M., and Garaebiti, E.: Ultraviolet Camera Measurements of Passive and Explosive (Strombolian) Sulphur Dioxide Emissions at Yasur Volcano, Vanuatu, Remote Sensing, 12, 2703, https://doi.org/10.3390/rs12172703, 2020.

INGV: Bollettino settimanale sul monitoraggio multiparametrico del vulcano Etna del 11/02/2025, Tech. Rep. 07/2025 ETNA, Istituto Nazionale di Geofisica e Vulcanologia, https://www.ct.ingv.it/index.php/monitoraggio-e-sorveglianza/prodotti-del-monitoraggio/bollettini-settimanali-multidisciplinari/986-bollettino-Settimanale-sul-monitoraggio-vulcanico-geochimico-e-sismico-del-vulcano-Etna-del-2025-02-11/file, 2025a.

INGV: Bollettino settimanale sul monitoraggio multiparametrico del vulcano Etna del 18/02/2025, Tech. Rep. 08/2025 ETNA, Istituto Nazionale di Geofisica e Vulcanologia, https://www.ct.ingv.it/index.php/monitoraggio-e-sorveglianza/prodotti-del-monitoraggio/bollettini-settimanali-multidisciplinari/987-bollettino-Settimanale-sul-monitoraggio-vulcanico-geochimico-e-sismico-del-vulcano-Etna-del-2025-02-18/file, 2025b.

INGV: Bollettino settimanale sul monitoraggio multiparametrico del vulcano Etna del 25/02/2025, Tech. Rep. 09/2025 ETNA, Istituto Nazionale di Geofisica e Vulcanologia, https://www.ct.ingv.it/index.php/monitoraggio-e-sorveglianza/prodotti-del-monitoraggio/bollettini-settimanali-multidisciplinari/990-bollettino-Settimanale-sul-monitoraggio-vulcanico-geochimico-e-sismico-del-vulcano-Etna-del-2025-02-25/file, 2025c.

INGV: Bollettino settimanale sul monitoraggio multiparametrico del vulcano Etna del 04/03/2025, Tech. Rep. 10/2025 ETNA, Istituto Nazionale di Geofisica e Vulcanologia, https://www.ct.ingv.it/index.php/monitoraggio-e-sorveglianza/prodotti-del-monitoraggio/bollettini-settimanali-multidisciplinari/991-bollettino-Settimanale-sul-monitoraggio-vulcanico-geochimico-e-sismico-del-vulcano-Etna-del-2025-03-04/file, 2025d.

INGV: Bollettino settimanale sul monitoraggio multiparametrico del vulcano Etna del 11/03/2025, Tech. Rep. 11/2025 ETNA, Istituto Nazionale di Geofisica e Vulcanologia, https://www.ct.ingv.it/index.php/monitoraggio-e-sorveglianza/prodotti-del-monitoraggio/bollettini-settimanali-multidisciplinari/994-bollettino-Settimanale-sul-monitoraggio-vulcanico-geochimico-e-sismico-del-vulcano-Etna-del-2025-03-11/file, 2025e.

Kilgour, G., Gates, S., Kennedy, B., Farquhar, A., McSporran, A., and Asher, C.: Phreatic eruption dynamics derived from deposit analysis: a case study from a small, phreatic eruption from Whakāri/White Island, New Zealand, Earth, Planets and Space, 71, 36, https://doi.org/10.1186/s40623-019-1008-8, 2019.

Kirby, J., Chapman, L., and Chapman, V.: Assessing the Raspberry Pi as a low-cost alternative for acquisition of near infrared hemispherical digital imagery, Agricultural and Forest Meteorology, 259, 232–239, https://doi.org/10.1016/j.agrformet.2018.05.004, 2018.

Manzella, I., Bonadonna, C., Phillips, J. C., and Monnard, H.: The role of gravitational instabilities in deposition of volcanic ash, Geology, 43, 211–214, https://doi.org/10.1130/G36252.1, 2015.

Mastin, L. G., Guffanti, M., Servranckx, R., Webley, P., Barsotti, S., Dean, K., Durant, A., Ewert, J. W., Neri, A., Rose, W. I., Schneider, D., Siebert, L., Stunder, B., Swanson, G., Tupper, A., Volentik, A., and Waythomas, C. F.: A multidisciplinary effort to assign realistic source parameters to models of volcanic ash-cloud transport and dispersion during eruptions, Journal of Volcanology and Geothermal Research, 186, 10–21, https://doi.org/10.1016/j.jvolgeores.2009.01.008, 2009.

Mathe, S. E., Kondaveeti, H. K., Vappangi, S., Vanambathina, S. D., and Kumaravelu, N. K.: A comprehensive review on applications of Raspberry Pi, Computer Science Review, 52, 100 636, https://doi.org/10.1016/j.cosrev.2024.100636, 2024.

Miikki, K., Karako?, A., Rafiee, M., Lee, D. W., Vapaavuori, J., Tersteegen, J., Lemetti, L., and Paltakari, J.: An open-source camera system for experimental measurements, SoftwareX, 14, 100 688, https://doi.org/10.1016/j.softx.2021.100688, 2021.

Mingotti, N. and Woods, A. W.: Video-based measurements of the entrainment, speed and mass flux in a wind-blown eruption column, Communications Earth & Environment, 5, 1–10, https://doi.org/10.1038/s43247-024-01402-x, 2024.

Moure, D., Torres, P., Casas, B., Toma, D., Blanco, M. J., Del Río, J., and Manuel, A.: Use of Low-Cost Acquisition Systems with an Embedded Linux Device for Volcanic Monitoring, Sensors, 15, 20 436–20 462, https://doi.org/10.3390/s150820436, 2015.

Nguyen, H.-Q., Loan, T. T. K., Mao, B. D., and Huh, E.-N.: Low cost real-time system monitoring using Raspberry Pi, in: 2015 Seventh International Conference on Ubiquitous and Future Networks, pp. 857–859, https://doi.org/10.1109/ICUFN.2015.7182665, 2015.

https://doi.org/10.5194/egusphere-2026-4353
Preprint. Discussion started: 11 August 2026

Parcheta, C. E., Pavlov, C. A., Wiltsie, N., Carpenter, K. C., Nash, J., Parness, A., and Mitchell, K. L.: A robotic approach to mapping post-eruptive volcanic fissure conduits, Journal of Volcanology and Geothermal Research, 320, 19–28, https://doi.org/10.1016/j.jvolgeores.2016.03.006, 2016.

Patrick, M. R., Kauahikaua, J. P., and Antolik, L.: MATLAB tools for improved characterization and quantification of volcanic incandescence in Webcam imagery: Applications at Kilauea Volcano, Hawaii, US Geol. Surv. Tech. Methods, 13, 1–16, https://doi.org/10.3133/tm13A1, 2010.

Patrick, M. R., Orr, T. R., Lee, L., and Moniz, C. J.: A multipurpose camera system for monitoring K¯ ilauea Volcano, Hawai'i, Tech. Rep. 13-A2, U.S. Geological Survey, https://pubs.usgs.gov/publication/tm13A2, 2015.

Patrick, M. R., Dietterich, H. R., Lyons, J. J., Diefenbach, A. K., Parcheta, C., Anderson, K. R., Namiki, A., Sumita, I., Shiro, B., and Kauahikaua, J. P.: Cyclic lava effusion during the 2018 eruption of Kīlauea Volcano, Science, 366, eaay9070, https://doi.org/10.1126/science.aay9070, publisher: American Association for the Advancement of Science, 2019.

Pering, T. D., Wilkes, T. C., Layana, S., Aguilera, F., and Aguilera, M.: The PiGas: A low-cost approach to volcanic gas sampling, Journal of Volcanology and Geothermal Research, 449, 108 063, https://doi.org/10.1016/j.jvolgeores.2024.108063, 2024.

Phillips, J. C., Barclay, J., Pyle, D. M., Armijos, M. T., Few, R., and Hicks, A.: Dynamic and Extensive Risk Arising from Volcanic Ash Impacts on Agriculture, Tech. rep., United Nations Office for Disaster Risk Reduction, 2019.

Prata, F., Corradini, S., Biondi, R., Guerrieri, L., Merucci, L., Prata, A., and Stelitano, D.: Applications of Ground-Based Infrared Cameras for Remote Sensing of Volcanic Plumes, Geosciences, 14, 82, https://doi.org/10.3390/geosciences14030082, 2024.

Prinz, A. C. B., Taank, V. K., Voegeli, V., and Walters, E. L.: A novel nest-monitoring camera system using a Raspberry Pi micro-computer, Journal of Field Ornithology, 87, 427–435, https://doi.org/10.1111/jofo.12182, 2016.

Ricco, C., Aquino, I., Augusti, V., D'Auria, L., Del Gaudio, C., and Scarpato, G.: Improvement and development of the tiltmetric monitoring networks of Neapolitan volcanoes, Ann. Geophys, 61, https://doi.org/10.4401/ag-7496, 2018.

Risacher, D. and Craig, I.: Sunwait, https://github.com/risacher/sunwait, 2022.

Sarıyer, R. M., Edwards, A. D., and Needs, S. H.: Open Hardware for Microfluidics: Exploiting Raspberry Pi Singleboard Computer and Camera Systems for Customisable Laboratory Instrumentation, Biosensors, 13, 948, https://doi.org/10.3390/bios13100948, 2023.

Scollo, S., Prestifilippo, M., Pecora, E., Corradini, S., Merucci, L., Spata, G., and Coltelli, M.: Eruption column height estimation of the 2011-2013 Etna lava fountains, Annals of Geophysics, 57, S0214–S0214, https://doi.org/10.4401/ag-6396, 2014.

Simionato, R.: PlumeTraP, doi:10.5281/zenodo.10970679, 2024.

Simionato, R.: rpiCamNodes, https://doi.org/10.5281/zenodo.21454039, 2026.

Simionato, R., Jarvis, P. A., Rossi, E., and Bonadonna, C.: PlumeTraP: A New MATLAB-Based Algorithm to Detect and Parametrize Volcanic Plumes from Visible-Wavelength Images, Remote Sensing, 14, 1766, https://doi.org/10.3390/rs14071766, 2022.

Simionato, R., Jarvis, P. A., Rossi, E., Fries, A., Pistolesi, M., Aguilar, R., and Bonadonna, C.: Combining visible- and infrared/wavelength observations with numerical modelling to describe Vulcanian eruption plumes at Sabancaya, Peru, https://doi.org/10.5281/zenodo.10891512, 2024.

Simionato, R., Fries, A., Thivet, S., Lemus, J., Díaz-Vecino, C., Arlaud, F., Scollo, S., and Bonadonna, C.: Dataset supporting "A cost-effective, open-source, high-resolution visible-wavelength camera network: design and applications for long-term monitoring and research in volcanology", https://doi.org/10.5281/zenodo.21224285, 2026.

Snee, E., Jarvis, P. A., Simionato, R., Scollo, S., Prestifilippo, M., Degruyter, W., and Bonadonna, C.: Image analysis of volcanic plumes: A simple calibration tool to correct for the effect of wind, Volcanica, 6, 447–458, https://doi.org/10.30909/vol.06.02.447458, 2023.

https://doi.org/10.5194/egusphere-2026-4353
Preprint. Discussion started: 11 August 2026

Sork, A. R., Kennedy, B. M., Watson, L., Taddeucci, J., Fitzgerald, R., Sellier, M., Biensan, C., Andronico, D., Scarlato, P., Bello, E. D., and Ricci, T.: Size matters: A new view of the relationship between shape and size for molten volcanic ballistics., https://doi.org/10.21203/rs.3.rs-4877945/v1, 2024.

Spence, R. J. S., Kelman, I., Baxter, P. J., Zuccaro, G., and Petrazzuoli, S.: Residential building and occupant vulnerability to tephra fall, Natural Hazards and Earth System Sciences, 5, 477–494, https://doi.org/10.5194/nhess-5-477-2005, 2005.

Stewart, C., Johnston, D. M., Leonard, G. S., Horwell, C. J., Thordarson, T., and Cronin, S. J.: Contamination of water supplies by volcanic ashfall: A literature review and simple impact modelling, Journal of Volcanology and Geothermal Research, 158, 296–306, https://doi.org/10.1016/j.jvolgeores.2006.07.002, 2006.

Taddeucci, J., Alatorre-Ibargüengoitia, M. A., Cruz-Vázquez, O., Del Bello, E., Scarlato, P., and Ricci, T.: In-flight dynamics of volcanic ballistic projectiles, Reviews of Geophysics, 55, 675–718, https://doi.org/10.1002/2017RG000564, 2017.

Tarquini, S., Isola, I., Favalli, M., Battistini, A., and Dotta, G.: TINITALY, a digital elevation model of Italy with a 10 meters cell size, version 1.1, https://doi.org/10.13127/TINITALY/1.1, 2023.

Thivet, S., Bagheri, G., Kornatowski, P. M., Fries, A., Lemus, J., Simionato, R., Díaz-Vecino, C., Rossi, E., Yamada, T., Scollo, S., and Bonadonna, C.: In situ volcanic ash sampling and aerosol–gas analysis based on UAS technologies (AeroVolc), Atmospheric Measurement Techniques, 18, 2803–2824, https://doi.org/10.5194/amt-18-2803-2025, 2025.

Thivet, S., Simionato, R., Fries, A., Díaz-Vecino, C., Lemus, J., Fréret-Lorgeril, V., Poulidis, A. P., Iguchi, M., and Bonadonna, C.: In-situ evidence of volcanic ash aggregation during fallout from combined ground- and UAS-based observations, Scientific Reports, https://doi.org/10.1038/s41598-026-45460-x, 2026.

Valade, S. A., Harris, A. J. L., and Cerminara, M.: Plume Ascent Tracker: Interactive Matlab software for analysis of ascending plumes in image data, Computers & Geosciences, 66, 132–144, https://doi.org/10.1016/j.cageo.2013.12.015, 2014.

Wilkes, T. C., McGonigle, A. J. S., Pering, T. D., Taggart, A. J., White, B. S., Bryant, R. G., and Willmott, J. R.: Ultraviolet Imaging with Low Cost Smartphone Sensors: Development and Application of a Raspberry Pi-Based UV Camera, Sensors, 16, 1649, https://doi.org/10.3390/s16101649, 2016.

Wilkes, T. C., Pering, T. D., McGonigle, A. J. S., Tamburello, G., and Willmott, J. R.: A Low-Cost Smartphone Sensor-Based UV Camera for Volcanic SO2 Emission Measurements, Remote Sensing, 9, 27, https://doi.org/10.3390/rs9010027, 2017.

Wilkes, T. C., Stanger, L. R., Willmott, J. R., Pering, T. D., McGonigle, A. J. S., and England, R. A.: The Development of a Low-Cost, Near Infrared, High-Temperature Thermal Imaging System and Its Application to the Retrieval of Accurate Lava Lake Temperatures at Masaya Volcano, Nicaragua, Remote Sensing, 10, 450, https://doi.org/10.3390/rs10030450, 2018.

Wilkes, T. C., Pering, T. D., McGonigle, A. J. S., Willmott, J. R., Bryant, R., Smalley, A. L., Mims, F. M., Parisi, A. V., and England, R. A.: The PiSpec: A Low-Cost, 3D-Printed Spectrometer for Measuring Volcanic SO2 Emission Rates, Frontiers in Earth Science, 7, https://doi.org/10.3389/feart.2019.00065, 2019.

Wilkes, T. C., Pering, T. D., and McGonigle, A. J. S.: Semantic segmentation of explosive volcanic plumes through deep learning, Computers & Geosciences, 168, 105 216, https://doi.org/10.1016/j.cageo.2022.105216, 2022.

Wilkinson, M., Bell, M. C., and Morison, J. I. L.: A Raspberry Pi-based camera system and image processing procedure for low cost and long-term monitoring of forest canopy dynamics, Methods in Ecology and Evolution, 12, 1316–1322, https://doi.org/10.1111/2041-210X.13610, 2021.

https://doi.org/10.5194/egusphere-2026-4353
Preprint. Discussion started: 11 August 2026

Wilson, T. M., Cole, J. W., Stewart, C., Cronin, S. J., and Johnston, D. M.: Ash storms: impacts of wind-remobilised volcanic ash on rural communities and agriculture following the 1991 Hudson eruption, southern Patagonia, Chile, Bulletin of Volcanology, 73, 223–239, https://doi.org/10.1007/s00445-010-0396-1, 2011.

Wilson, T. M., Stewart, C., Sword-Daniels, V., Leonard, G. S., Johnston, D. M., Cole, J. W., Wardman, J., Wilson, G., and Barnard, S. T.: Volcanic ash impacts on critical infrastructure, Physics and Chemistry of the Earth, Parts A/B/C, 45-46, 5–23, https://doi.org/10.1016/j.pce.2011.06.006, 2012.

Woodhouse, M. J., Hogg, A. J., Phillips, J. C., and Sparks, R. S.: Interaction between volcanic plumes and wind during the 2010 Eyjafjallajökull eruption, Iceland, Journal of Geophysical Research: Solid Earth, 118, 92–109, https://doi.org/10.1029/2012JB009592, 2013.